Electronic Supplementary Material (ESI) for Energy & Environmental Science.


# The anisotropy of the carrier diffusion in single $MAPbI_3$ grains correlates to their twin domains

Ilka M. Hermes,[a, *] Andreas Best,[a] Leonard Winkelmann,[a,c] Julian Mars,[a] Sarah M. Vorpahl,[b] Markus Mezger,[a, c] Liam Collins,[d] Hans-Jürgen Butt,[a] David S. Ginger,[b] Kaloian Koynov[a] and Stefan A. L. Weber[a, c, *]

[a] Max Planck Institute for Polymer Research, Ackermannweg 10, 55128 Mainz, Germany

[b] Department of Chemistry, University of Washington, Seattle, Washington 98105, United States

[c] Institute of Physics, Johannes Gutenberg University Mainz, Duesbergweg 10-14, 55128 Mainz, Germany

[d] Center for Nanophase Materials Sciences, Oak Ridge National Laboratory, 1 Bethel Valley Rd., Oak Ridge, Tennessee 37830, USA

**Corresponding Authors**

* Ilka M. Hermes, Email: hermesi@mpip-mainz.mpg.de and Stefan A. L. Weber, Email: webers@mpip-mainz.mpg.de

**Figure S1**

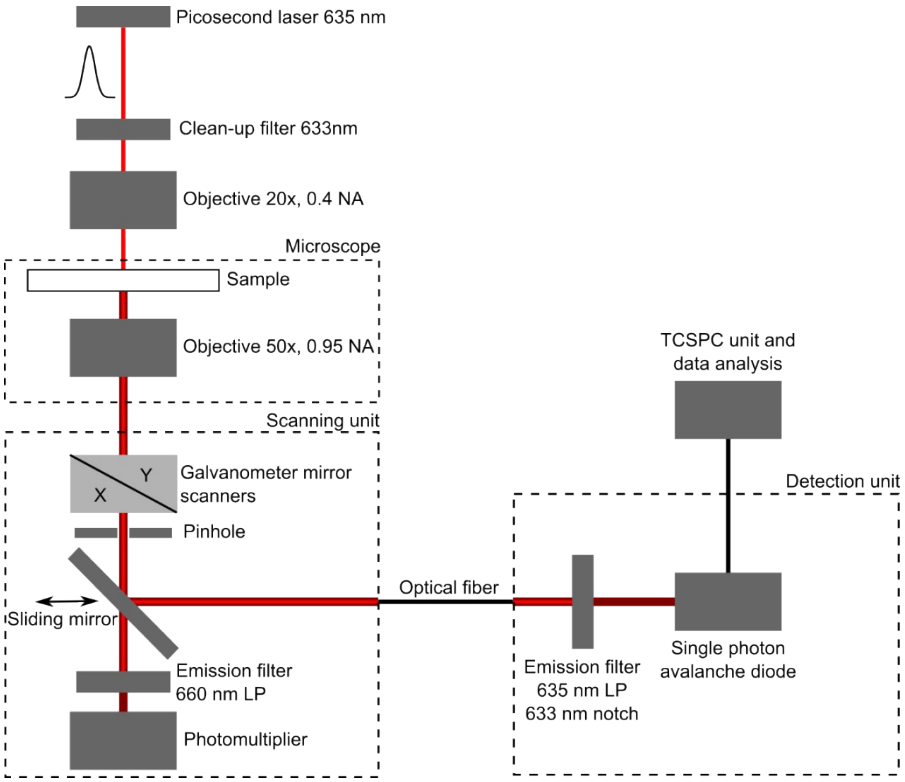


Figure S1: Beam path schematic of the spatial- and time-resolved PL setup with the optical excitation with a picosecond laser from the top and the detection of the PL emission in transmission either by a photomultiplier for the static PL distribution, scanned by XY galvanometer-mirrors, or by a detection unit from PicoQuant with a τ-SPAD avalanche diode followed by TCSPC unit. The experimental setup is described in depth in the methods section.

## Figure S2

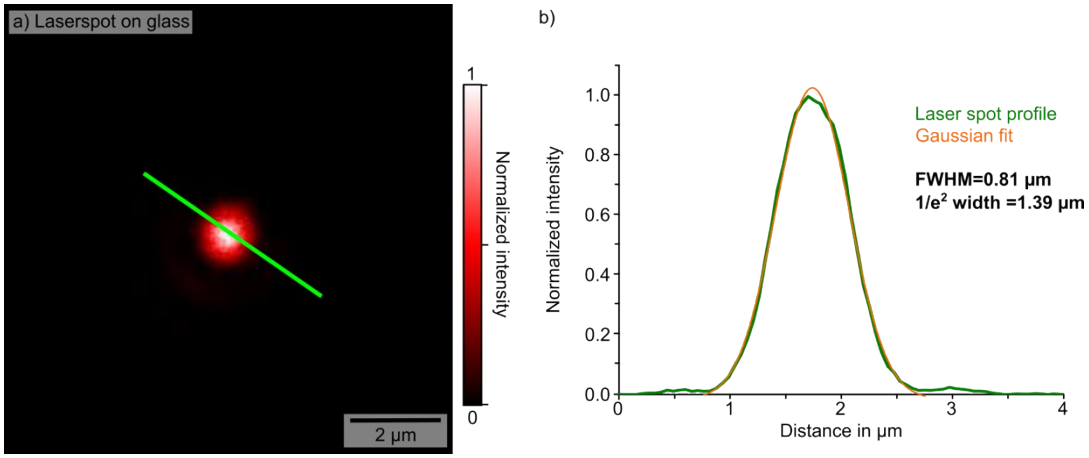


Figure S2: Diameter of the excitation spot measured on glass in transmission with the galvanometer mirror scanners without the 660 nm LP emission filter (excitation fluence of 0.77 µJ/cm², repetition rate of 2 MHz, pinhole 60 µm - comparable to the excitation during the time-resolved PL measurements). The intensity profile in b) was extracted at the positions of the green line in a) and fitted with a Gaussian function to determine the spot diameter at FWHM.

The diameter of the laser spot at full width half-maximum (FWHM) was determined by focusing the excitation spot onto the glass substrate next to the characterized $MAPbI_3$ grain with the same excitation parameters used during the time-resolved PL measurements. We fitted the intensity profile extracted at the position of the green line in Figure S2a with a Gaussian peak function and found a beam diameter of 0.81 µm at FWHM (Figure S2b).

## Discussion S3

For the calculation of the approximate initial carrier density, we measured the average laser power for each of the experimental settings to calculate the respective fluence (energy density) given in the table below.

To calculate the initial carrier density $N_0$ from the fluence we used the following equation according to Richter et al.[1]

$$N_0 = \frac{fluence * a}{E_{ph} * t}$$

With an absorbtance $a$~0.5, a photon energy $E_{ph}$= 3.14 *$10^{-19}$ J and a thickness $t$ of ~1000 nm. The penetration depth was around 400 nm.[2]

| Average power in nW<br>Repetition rate: 2 MHz | Pulse energy in fJ | Energy density in µJ/cm² | Carrier density in 1/cm³ |
|---|---|---|---|
| 23.6 | 11.8 | 0.772 | 1.23 * $10^{16}$ |
| 26.6 | 13.3 | 0.870 | 1.39 * $10^{16}$ |
| 27.3 | 13.7 | 0.893 | 1.43 * $10^{16}$ |
| 28.6 | 14.3 | 0.936 | 1.49 * $10^{16}$ |
| Average power in nW<br>Repetition rate: 20 MHz | Pulse energy in fJ | Energy density in µJ/cm² | |
| 214 | 10.7 | 0.700 | 1.12 * $10^{16}$ |
| 254 | 12.7 | 0.831 | 1.33 * $10^{16}$ |
| 260 | 13.0 | 0.851 | 1.36 * $10^{16}$ |
| 267 | 13.3 | 0.874 | 1.40 * $10^{16}$ |

## Figure S4

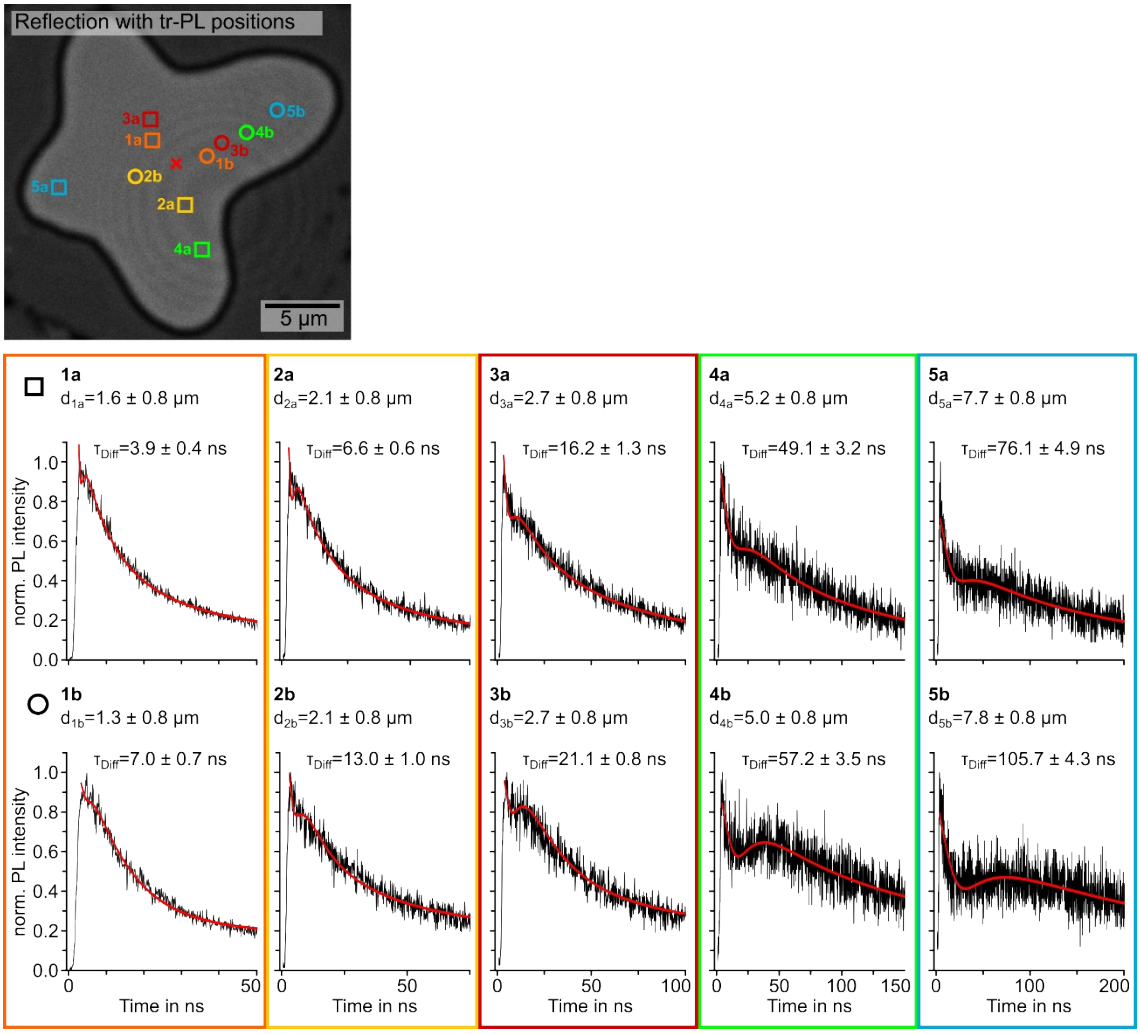


Figure S4: Additional time-resolved PL decays measured in various distances from the excitation spot detected along different directions of the grain marked in the PL reflection image by the colored squares and circles. Each color represents two detection positions at comparable distances, with the squares (a) marking the direction of shorter diffusion times and the circles (b) marking the direction of longer diffusion times. Position of the excitation with a pulsed picosecond laser with fluence 0.77 µJ/cm² and a repetition rate of 2 MHz is marked by the red cross. The data fits of the according PL decays are displayed in red. Please note that the scales of the time-axis were changed to increase the comprehensibility of the shift of the diffusion peak.

The additional time-resolved PL decays in Figure S4 detected at two comparable distances from the excitation position, each, visualize the anisotropy of the diffusion time $\tau_{Diff}$. These decay curves are consistent with the findings presented in the main manuscript.

## Figure S5

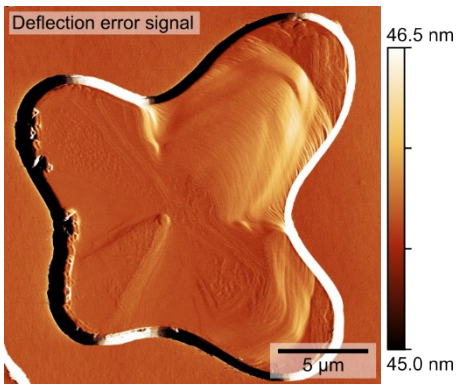


Figure S5: Deflection error signal of PFM measurement shown in Figure 3 in the main manuscript.

The deflection error signal in Figure S5 corresponding to the lateral PFM measurement in Figure 3 in the main manuscript shows the defined terrace steps indicating a high crystallinity.

## Figure S6

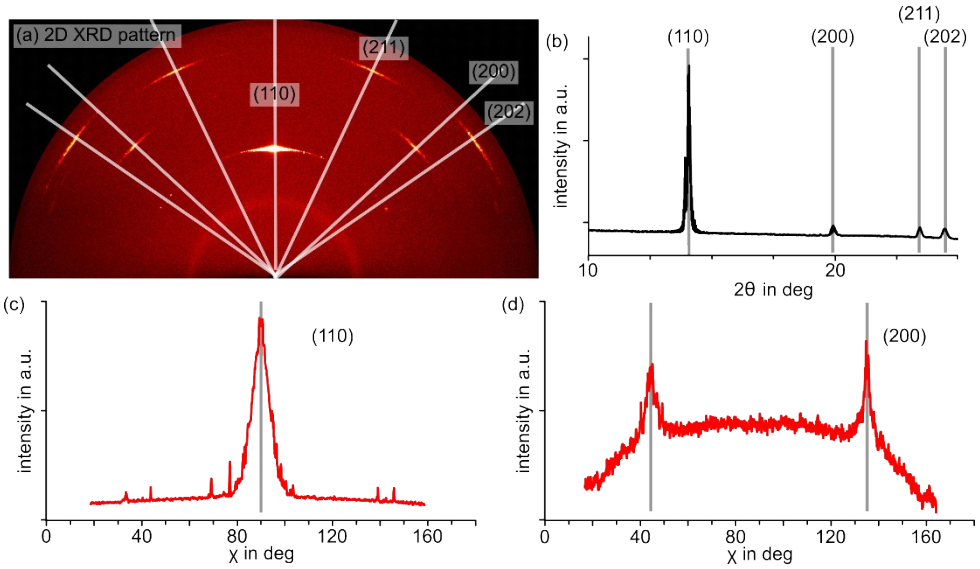


Figure S6: 2D XRD characterization of a $MAPbI_3$ thin film from the same batch as the sample in the main manuscript. a) 2D XRD pattern. b) 1D diffraction pattern from radially averaging the 2D pattern in a). c) Intensity distribution of the (110) and d) the (200) Bragg reflection vs. the azimuthal angle.

The 2D XRD pattern of a $MAPbI_3$ thin film from the same batch studied by PFM and PL shows distinct and pronounced Bragg reflections at the position of the (110), (200), (202) and (211) crystal planes (Figure S6a and S6b). The radially averaged diffraction pattern (Fig. S6b) exhibits a strong (110) reflection at 14.1° and weak reflections of the (200), (211) and (202) crystal plane at 19.9°, 23.5° and 24.5°, respectively. These Bragg angles 2θ are in good agreement with literature values reported for tetragonal $MAPbI_3$ perovskite.[3–5] The absence of the characteristic $PbI_2$ reflection between 12° and 13° suggests the absence of degradation products, despite the solvent annealing on air.

The intensity distributions of the (110) and (200) reflections show intensity maxima at the azimuthal angles X of 90° and 45° and 135°, respectively (Fig. S6c and d). Measurements at various incident angles confirm that the maximum of the (110) reflection was located around specular condition. This implies, that the (110) crystal plane is predominantly oriented parallel to the sample surface. Accordingly, the (202) and (211) Bragg reflections are positioned at the azimuthal angles expected for the sample surface oriented parallel to the (110) plane (white lines in Fig. S6a). We observed the same texture previously on similar $MAPbI_3$ perovskite films.[6]

## Figure S7

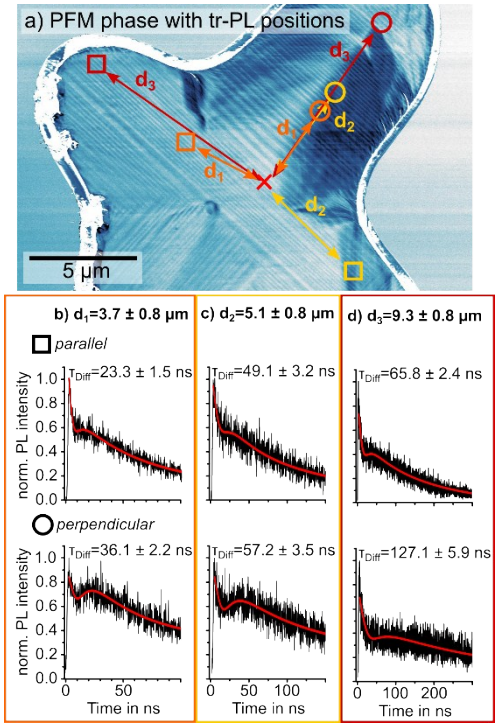


Figure S7: a) Lateral PFM phase image of the grain illustrating the detection positions of the six PL decays shown in b, c and d. These positions were selected at defined distances di from the excitation spot (red cross) in direction either parallel (squares) or perpendicular (circles) to the twin domains. b) PL decays detected at the position of the orange square and circle in a, with $d_1$=3.7±0.8 µm. c) PL decays detected at the position of the yellow square and circle in a, with $d_2$=5.1±0.8 µm. d) PL decays detected at the position of the red square and circle in a, with $d_3$=9.3±0.8 µm. The red lines in b-d represent the corresponding fits according to eq.1. Please note that the scales of the time-axis change to increase the comprehensibility of the diffusion peak shift. Excitation with 633 nm wavelength, a fluence of 0.77 µJ/cm², a repetition rate of 2 MHz and 0.81 µm beam diameter (Figure S2).

## Figure S8

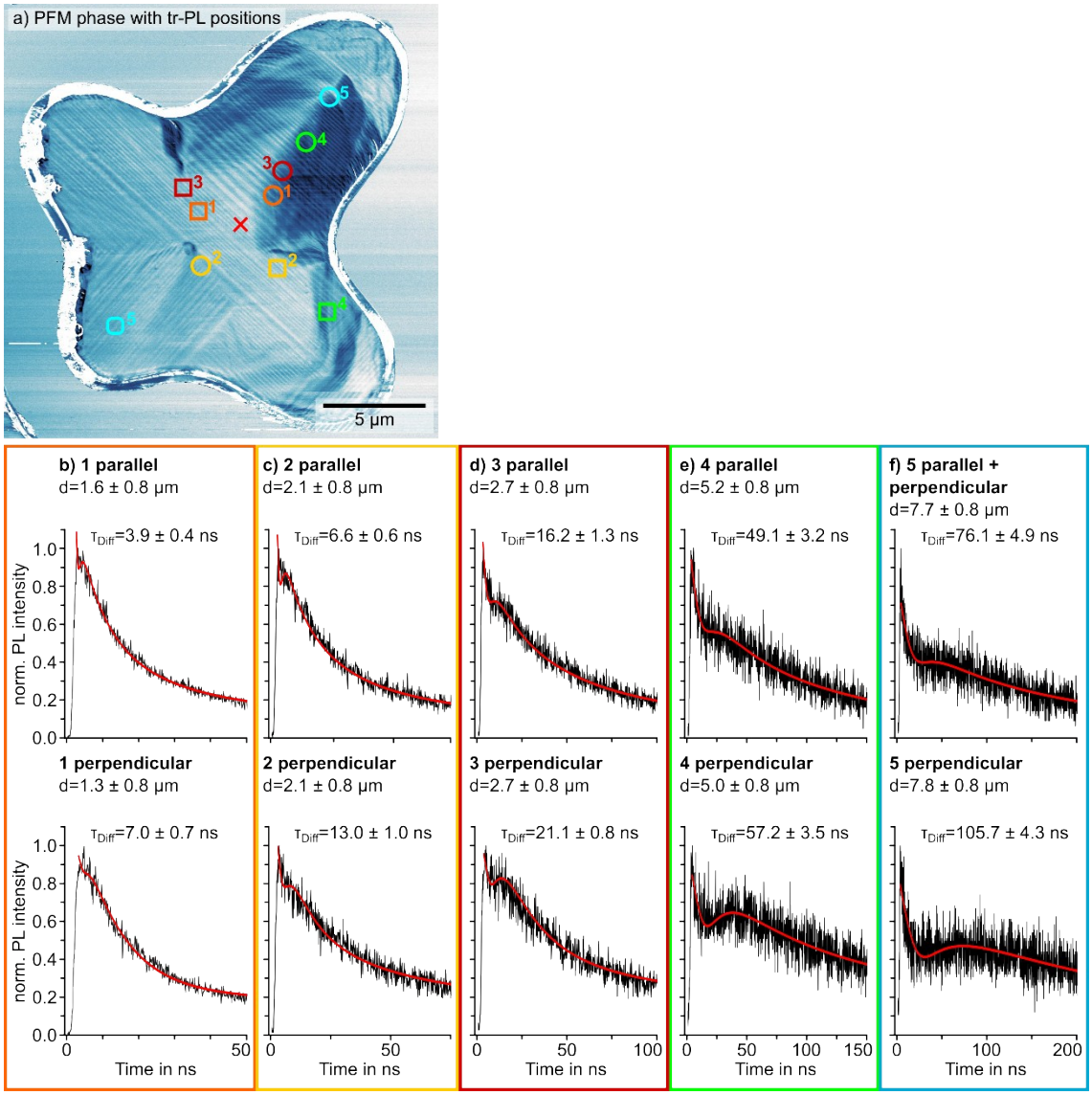


Figure S8: Correlation of time-resolved PL decays from Figure S4 with the ferroelastic domain pattern imaged in the PFM phase in a. PL decays were measured in various distances from the excitation spot detected along different directions of the grain marked in the PFM phase by the colored squares and circles. Each color represents two detection positions at comparable distances, with the squares marking a detection position parallel to the domains and the circles marking a detection position perpendicular to the domains. Position of the excitation with a pulsed picosecond laser with fluence 0.77 µJ/cm² and a repetition rate of 2 MHz is marked by the red cross. The data fits of the according PL decays are displayed in red. Please note that the scales of the time-axis were changed to increase the comprehensibility of the shift of the diffusion peak.

## Figure S9

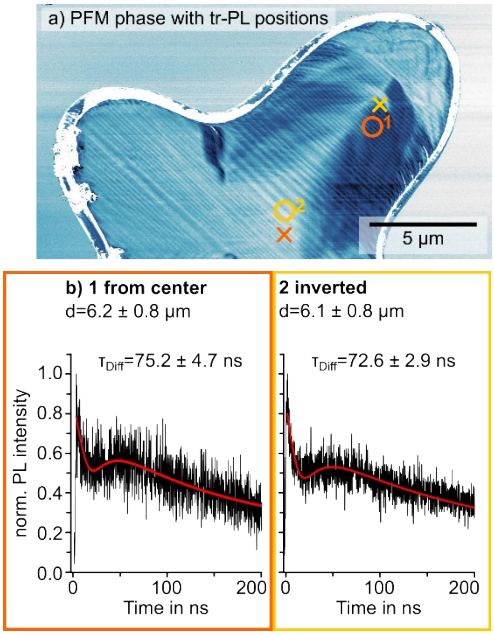


Figure S9: a) PFM phase with the detection positions of time-resolved PL decays marked by the orange and yellow numbered circles and the excitation positions marked by the orange and yellow cross for excitation from center and the inverted excitation and detection, respectively. Excitation with a pulsed picosecond laser with fluence 0.77 µJ/cm² and a repetition rate of 2 MHz. Time-resolved PL decays detected from center and inverted excitation and detection locations in are shown in b.

We find that diffusion times extracted from the PL decays with excitation position in the grain center and with inverted excitation and detection positions coincide. Thus, an influence of a macroscopic drift originating from the grain boundaries on the carrier diffusion can be excluded.

## Figure S10

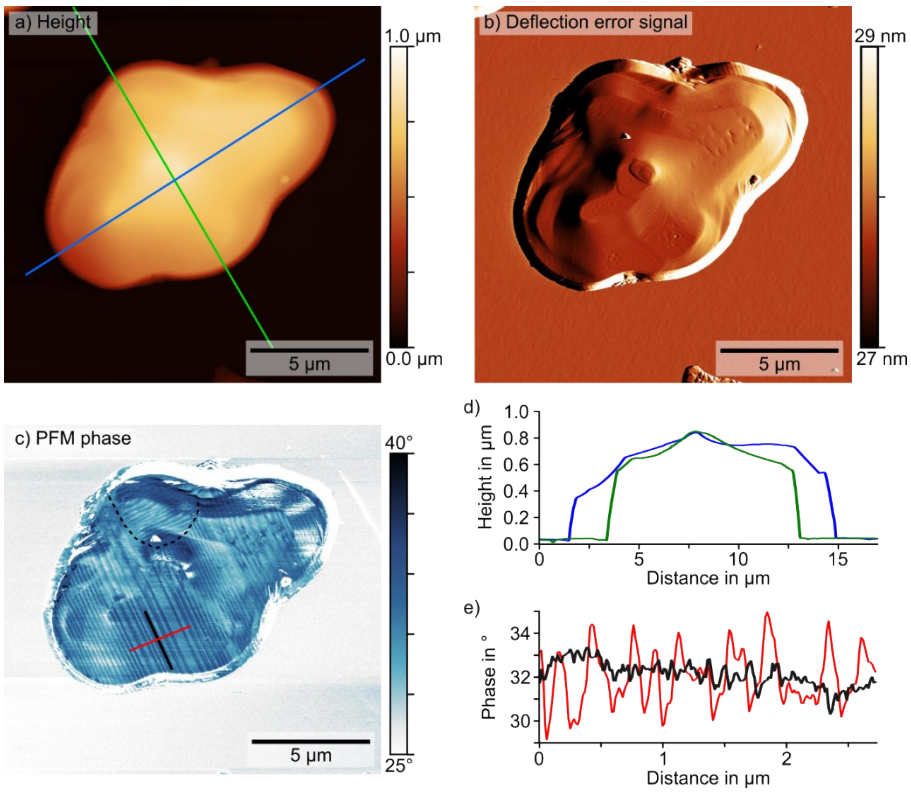


Figure S10: Lateral PFM measurement (1.5 V AC excitation, 736 kHz, 48 nN) on another large isolated $MAPbI_3$ grain of a thin film sample from the same batch as the sample characterized in the main manuscript and the sample used for XRD in the SI Figure S2. a) Height signal with positions of profiles (green and blue line) shown in d. b) Deflection error signal of PFM measurement. c) Lateral PFM phase imaging periodic twin domains with position of the profiles (solid black and red line) shown in e. The area with a 90° direction change is outlined with the dashed black line. d) Height profiles extracted at the position of the blue and green line in a show some step edges over a height of 0.3 - 0.4 µm in both profiles. e) PFM phase profiles extracted at the positions of the red and black line in c showing the absence of periodicity in the profile parallel to the domains along the black line and varying periodicities between 0.15 and 0.47 µm in the profile extracted perpendicular to the domains along the red line.

The PFM data of another $MAPbI_3$ grain from a sample of the same batch are summarized in Figure S10. Similar to the crystallite characterized in the main manuscript, we chose a large isolated grain to avoid additional inter-grain diffusion effects due to shared grain walls. The grain in Figure S10 is around 9 µm in diameter along its shorter axis (green line in a and d) and 13 µm along its long axis (blue line in a and d) with a surface area of 91 µm². The grain exhibits a terrace-like surface structure with smooth terrace surfaces and step edges located close to the center of the grain as well as close to the grain boundaries (S10b and d). The PFM phase in 10c clearly visualizes the periodic piezoresponse of the twin domains with a periodicity of 0.15 - 0.47 µm (S10e).

## Figure S11

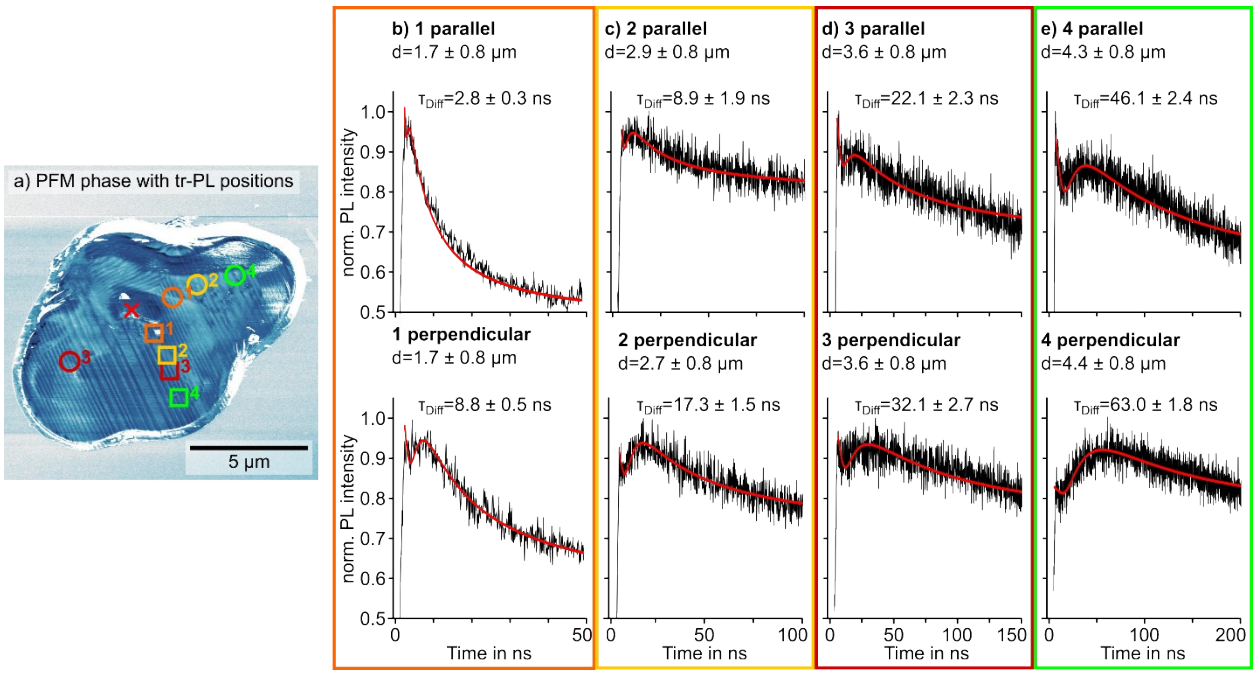


Figure S11: Time-resolved PL decays measured on a $MAPbI_3$ grain of another sample from the same batch, previously characterized via PFM in Figure S10. a) PFM phase with the detection positions of the time–resolved PL decays marked by the colored and numbered circles and squares in various distances from the excitation spot marked with the red cross. The circles represent detection positions perpendicular to the twin domains and the squares represent detection positions parallel to the twin domains. Excitation with a pulsed picosecond laser with fluence 0.77 µJ/cm² and a repetition rate of 2 MHz. The data fit is displayed in red. Please note that the scales of the time-axis were changed to increase the comprehensibility of the shift of the diffusion peak.

The time-resolved PL decays measured on a second large isolated $MAPbI_3$ grain of another sample from the same batch consistently exhibit a shift of the diffusion time to longer times for the carrier diffusion perpendicular to the twin domains, thus agreeing with the data presented in the main manuscript. Analogously to the PL decays in Figure 1, the shape of the PL decay originates from a superposition of an exponential decay wave-guided from the initial PL emission at the position of the excitation spot and a peak function from the carrier diffusion. The diffusion times $\tau_{Diff}$ are derived from the data fit as described in the main manuscript.

## Simulation S12

To clarify the impact of photon recycling on the deviations of the diffusion times at larger distances from a classical diffusion model, we performed a simple 1D Monte Carlo simulation. Starting from an initial ensemble of N=$10^8$ particles with a random Gaussian position distribution corresponding to the Gaussian beam profile, we iterated the distribution in timesteps of $\tau_{Step} = 5\ ns$ for 100 iterations (500 ns). We implemented the simulation in the software IgorPro 6.27 (Wavemetrics) using the built-in gnoise and expnoise functions. These functions generate random numbers with a Gaussian probability distribution of given characteristic width around zero (gnoise), or random positive numbers with an exponentially decaying probability distribution with characteristic decay length (expnoise).

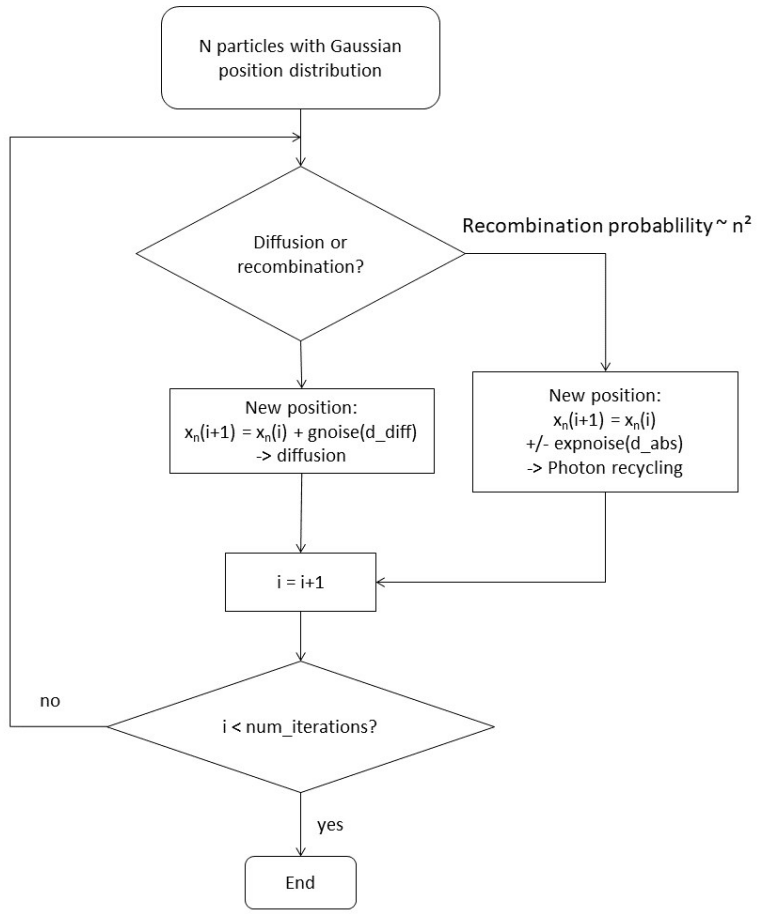


Figure S12 - 1: Sequence of 1D Monte-Carlo simulation on the influence of photon recycling o the detected diffusion times for large excitation-detection distances.

The sequence of the simulation is illustrated in Figure S12 - 1. For each step, the probability of bimolecular recombination $p_{BMrec}$ for a given particle is calculated from the particle density in the vicinity:

$$p_{BMrec} = k\ n^2$$

With a numerical prefactor k. If the particle falls into the recombination branch, the new position can be calculated via a Lambert-Beer absorption law with a characteristic absorption length of $\lambda_{Abs} = 1\mu m$. We assume that all the photons generated by bimolecular recombination are re-absorbed (i.e. photon recycling probability = 1), creating new particles at position

$$x_n(i+1) = x_n(i) \pm expnoise(\lambda_{Abs})$$

We want to point out that a photon-recycling probability of unity is unlikely, as many photons will escape the perovskite film via photoluminescence. Thus, our simulation captures a scenario with strong photon recycling.

All the particles that fall into the diffusion branch will diffuse over a characteristic distance $d_{diff} = \sqrt{2D\tau_{Step}}$ (with diffusion constant $D = 1\ cm^2/s$):

$$x_n(i+1) = x_n(i) + gnoise(d_{diff})$$

After each iteration in time, a histogram of the particle distribution is generated and added to a 2D contour plot of the particle density as a function of position and time (Figure S12 - 2). From these contour plots, we extracted particle density transients for given distances from the excitation. From the position of the maximum in these transients, we calculated the diffusion time for a given distance, similar to the analysis of the PL transients in the experimental data.

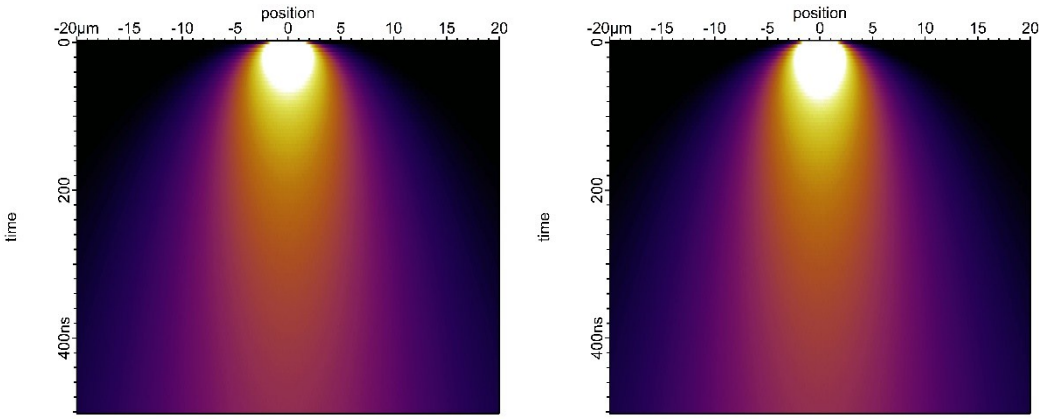


Figure S12 - 2: Particle density plots as function of position (horizontal) and time (vertical axis) for pure diffusion (left) and diffusion plus photon recycling (right). The brighter the color, the higher is the particle density.

From comparing the diffusion data with (k>0) and without (k=0) photon recycling we found that photon recycling slightly accelerates the effective diffusion. However, the effect is comparatively small (Figure S12-3), despite the fact that we used a rather high prefactor k to calculate the bimolecular recombination probability. We chose k to be high enough that after the first timestep, almost all particles recombine. Nevertheless, the particle density, $n$, decreases so rapidly within the first couple of nanoseconds that photon recycling due to the $n^2$- dependence of bimolecular recombination becomes so unlikely, that it does not affect the effective diffusion times any more (Figure S12-3). Therefore, the fits of the diffusion times versus the distance with and without photon recycling almost coincide. They yielded similar values for the effective bimolecular recombination coefficient $k_2 = 9352 \pm 23$ with photon recycling and $k_2 = 9882 \pm 23$ without photon recycling.

Concluding, we found that the influence of photon recycling at the given excitation energies on the effective diffusion times is minor and likely does not account for the observed deviation from the classic diffusion model at larger distances (Figure 4).

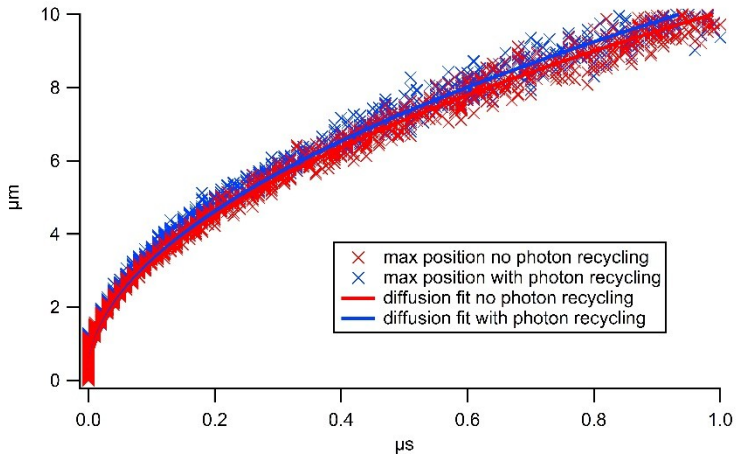

Figure S12 - 3: Diffusion times vs. distance between excitation and detection without photon recycling (red) and with photon recycling (blue).

## Figure S13

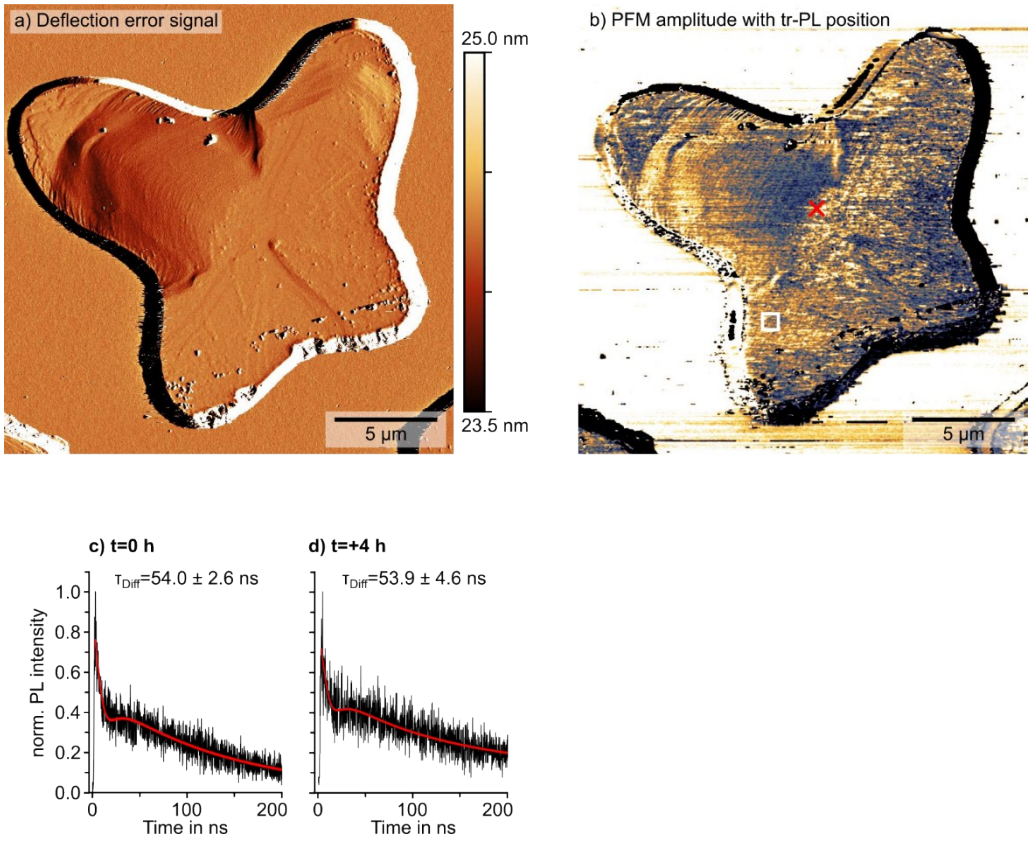


Figure S13: Lateral PFM measurement (1.5 V AC excitation, 777 kHz, 48 nN) after the PL measurements with the deflection error signal in a) and the PFM amplitude in b). Time-resolved PL decays measured at the same position of the white square in b from the excitation after a time of 0 (c) and 4 hours (d). Excitation with a pulsed picosecond laser (633 nm wavelength, 0.81 µm FWHM, 2 MHz and 0.7 µJ/cm² fluence).

To study the influence of possible degradation over the measurement time, we measured PFM on the same grain following the PL experiments. In the deflection error signal in S13a, we observe that the surface of the sample became rougher, compared to the measurement prior to the PL experiments in Figure 3. The PFM signal in S13b shows an increase in topographic crosstalk with PFM measurement due to the rougher sample surface. While the PFM signal becomes weaker, the overall structure of the twin domain remains unchanged. We suggest that the passivation of the sample surface weakened the resulting PFM signal. Since the domain arrangement remains and we detect the PL emission in transmission, we are confident that the surface passivation does not influence the PL data collection. To further confirm the benign influence of the surface passivation, we compared the PL decay of the same positions at the beginning and the end of the experiment. While we observe an increase in the noise level after 4 hours, the overall shape and the diffusion time of the PL decay remain unchanged, confirming negligible influence of degradation over the course of the experiments.

1 J. M. Richter, M. Abdi-Jalebi, A. Sadhanala, M. Tabachnyk, J. P. H. Rivett, L. M. Pazos-Outón, K. C. Gödel, M. Price, F. Deschler and R. H. Friend, *Nat. commun.*, 2016, **7**, 1–8.

2 S. De Wolf, J. Holovsky, S.-J. Moon, P. Löper, B. Niesen, M. Ledinsky, F.-J. Haug, J.-H. Yum and C. Ballif, *J. Phys. Chem. Lett.*, 2014, **5**, 1035–1039.

3 T. Baikie, Y. Fang, J. M. Kadro, M. Schreyer, F. Wei, S. G. Mhaisalkar, M. Graetzel and T. J. White, *J. Mater. Chem. A*, 2013, **1**, 5628–5641.

4 Z. Song, S. C. Watthage, A. B. Phillips, B. L. Tompkins, R. J. Ellingson and M. J. Heben, *Chem. Mater.*, 2015, **27**, 4612–4619.

5 J. A. Christians, P. A. Miranda Herrera and P. V Kamat, *J. Am. Chem. Soc.*, 2015, **137**, 1530–1538.

6 I. M. Hermes, S. A. Bretschneider, V. W. Bergmann, D. Li, A. Klasen, J. Mars, W. Tremel, F. Laquai, H.-J. Butt, M. Mezger, R. Berger, B. J. Rodriguez and S. A. L. Weber, *J. Phys. Chem. C*.